Applied Thermal Engineering 128 (2018) 672–683

Contents lists available at ScienceDirect

Applied Thermal Engineering

journal homepage: www.elsevier.com/locate/apthermeng

Research Paper

Comparative study of pool boiling heat transfer from various microchannel geometries

Avdhoot Walunj *, A. Sathyabhama

Department of Mechanical Engineering, National Institute of Technology Karnataka, Surathkal 575025, India

HIGHLIGHTS

- A new microchannel design i.e. stepped microchannel is introduced.
- Heat transfer mechanism in rectangular, parabolic, stepped microchannel is studied.
- Compound effect of channel profile and channel top width is studied.
- Bubble departure diameter and bubble frequency in the microchannel is quantified.
- The semi-analytical model is developed to estimate the bubble departure diameter.

ARTICLE INFO

Article history:
Received 19 May 2017
Revised 31 July 2017
Accepted 30 August 2017
Available online 6 September 2017

Keywords:
Open microchannel
Heat transfer enhancement
Bubble departure diameter
Bubble frequency
Incipient temperature

ABSTRACT

This paper presents the experimental investigation of pool boiling heat transfer enhancemrent using open microchannels. Rectangular, parabolic and stepped microchannels are fabricated on the 10 mm diameter circular copper test piece and their boiling characteristics are compared with that of the plain surface at saturated condition of distilled water. The effect of channel shape and geometrical parameter on the boiling heat transfer is studied. The channel top width and channel base width are varied from 250 μm to 500 μm and 500 μm to 800 μm, respectively. The fin tip thickness is varied from 200 μm to 500 μm. The channel height is fixed at 500 μm. The morphology of bubble is observed by using high-speed camera. Compound study of bubble departure diameter and bubble frequency has proved the significant performance of parabolic and stepped microchannel. All the microchannel geometries enhanced the heat transfer rate. The modification of rectangular channel into parabolic and stepped microchannel resulted in the maximum of 88% and 169% enhancement, respectively at 11.7 °C wall superheat. At heat flux of 100 kW/m^2, the heat transfer coefficient increased by 21.49–35.37% for different microchannels. The incipient temperature reduced by 13.72–23.18%. A semi-analytical model is developed to estimate the bubble departure diameter of the microchannel which predicts the present experimental data with mean absolute error of 5.58%.

1. Introduction

Failure mechanisms in electronic devices, such as inter-metallic growth, metal migration, and void formation are related to thermal defects. The generated heat may decrease the performance of the systems since almost every engineering system is designed to work within a certain temperature limit. Excessive heat generation beyond the limit could lead to system failure. At the same time, designing a compact arrangement is a challenge for engineers. Therefore, devising an efficient cooling solution to meet these challenges is of paramount importance and has direct impact on the performance and reliability of the electronic device.

Immersion cooling by pool boiling has potential to dissipate a large amount of heat at considerable less wall superheat temperature and many enhancement techniques are implemented in this mode of heat transfer to improve the thermal performance of power electronic devices. Passive cooling technique like fin, microchannel, etc. are widely preferred to enhance the boiling performance because of its compatibility and cooling potential of miniaturized devices. Unlike the active technique e.g. surface vibration, this technique does not require an external power source to drive. It does not have any moving parts and thus it can offer noise free operation. Additionally, fabrication of microchannel geometry is easy and cost effective. A representative literature on

* Corresponding author.
E-mail address: aawalunj@gmail.com (A. Walunj).

http://dx.doi.org/10.1016/j.applthermaleng.2017.08.157
1359-4311/

Nomenclature

C_h	channel height (μm)
C_w	channel width (μm)
D_b	bubble departure diameter (mm)
f	bubble frequency (Hz)
f_t	fin tip thickness (μm)
h	heat transfer coefficient (W/m^2 K)
k_{cu}	thermal conductivity of copper (W/mK)
m	mass (kg)
N	number of channel
q''	heat Flux (W/m^2)
r	instantaneous bubble radius (mm)
S	fin spacing (μm)
T	temperature (°C)
U	uncertainty
W_b	channel base width (μm)
W_t	channel top width (μm)

Greek symbols

ΔT	wall superheat (°C)
σ	surface tension (N/m)
ρ	density (kg/m^3)

Subscripts

b	bubble
l	liquid

pool boiling enhancement using open microchannel are presented in the Table.1. Kandlikar and his research team [1–3,6–8] have done numerous experimental study on the rectangular microchannel and found significant enhancement in boiling heat transfer at low wall superheat. Jaikumar and Kandlikar [1] noticed the heat transfer enhancement of about 270% from the rectangular microchannel of porous fin-top compared to the plain surface. They also studied the cohesive effect of the channel width and channel height on the heat transfer. Cooke and Kandlikar [2,3] used deep reactive etching method to fabricate the microchannel. They observed that wider channel provides the highest heat transfer rate because it assists the growth of bubble population. They noticed that the microchannel with channel width = 375 μm, channel height = 400 μm and area augmentation factor = 2.30 has maximum heat transfer performance. Ghiu and Joshi [4] found the weak dependence of channel width on heat transfer performance of enhanced structure. They proved that the channel pitch has great influence on the ebullition and growth of the bubble. The existence of dynamic nature of internal evaporation was noticed by the existence of an oscillatory movement of the vapor slug over the top and bottom of the channel. Yu and Lu [5] studied, for the first time, the effect of area enhancement ratio on the critical heat flux (CHF). The effect of fin spacing and fin height on the heat transfer was examined. They found that closer and higher fins can offer the flow resistance to lift-off the growing bubble. Higher aspect ratio i.e. decrease in the fin spacing or increase in the fin height adversely affected on the boiling performance. Mehta and Kandlikar [6,7] tested cylindrical tubes with rectangular circumferential microchannel and investigated the effect of the horizontal and vertical orientation of the tubes on the heat flux. Heat transfer coefficient (HTC) at horizontal and vertical orientations was 129 kW/m^2 K and 109 kW/m^2 K, respectively at about 1093 kW/m^2 heat flux. Patil and Kandlikar [8] followed the hybrid technique of enhancement with microporous coating on the fin top. Microchannel of 500 μm and 762 μm channel width with fin width = 200 μm and channel height = 400 μm had the best performance with CHF = 3250 kW/m^2 and HTC = 995 kW/m^2 K, respectively. They found that the heat transfer rate increases with increase in the channel height. They concluded that HTC decreases up to certain value and again increases with the increasing channel width.

The literature presented above indicates that microchannels have great potential in increasing the pool boiling heat transfer. The objective of this work is to compare the pool boiling performance of rectangular, parabolic and stepped microchannels. It is also proved in the literature that wider channel improves the heat transfer. Hence the effect of channel top width to bottom width, as a parameter, on heat transfer will be studied. The investigation will also include the high speed imaging to understand the bubble morphology. Further, a semi-analytical model will be proposed to estimate the bubble departure diameter by force balance approach. The forces acting on the growing bubble will be considered as a function of geometrical parameters, fluid properties and wall superheat.

2. Experimentation

2.1. Experimental setup

The experimental setup comprises of rectangular chamber, test section assembly, condenser assembly and CCD camera, as shown in Fig. 1. The 250 × 400 × 200 mm^3 rectangular boiling chamber, made up of SS 316, is fitted with top and bottom flanges. The top flange has provision for liquid charging, condenser cooling water inlet and outlet. Bottom flange has provision to insert the test section into the chamber. The necessary openings are provided in the chamber for thermocouple and pressure transducer to measure the water temperature (T_f) and chamber pressure, respectively. An auxiliary heater of 500 W capacity is provided to maintain the water at saturation temperature during the experiments. The boiling chamber has four transparent sight glasses to observe and record the boiling phenomenon by high-speed camera. The National Instruments cDaq-9178 data acquisition system with NI-9213 temperature module is used to acquire the temperature readings.

2.2. Test section

Copper test piece of 10 mm diameter and 20 mm length is screw fitted on the heating block as shown in Fig. 2. Heating block is made of copper and has provision at the bottom to insert four cartridge heaters, each of 200 W capacity. Teflon insulation is provided to the heating block and test piece assembly. O-ring and silicon gasket are used between the Teflon block and the test piece which ensures the leak proof assembly. Complete assembly is inserted into the boiling chamber from the bottom flange. K-type sheathed thermocouples of 1 mm diameter are planted in the test piece at 2 mm, 6 mm and 10 mm from the top surface and the temperatures T_1, T_2 and T_3 correspond to these thermocouple readings, respectively.

Various types of microchannel are fabricated on the top circular surface of the test piece by wire EDM. Five test pieces with different microchannel dimensions and profile are fabricated to study the effect the geometrical parameters and channel profile on the

Table 1
Summary of literature.

Author	Base Material	Boiling Fluid	Characteristics	Fabrication Technique	Size/Shape/Type of the structure	CHF	HTC
Jaikumar and Kandlikar [1]	Cu	DI water	Microchannel + porous fin top	Sintering, CNC	Rectangular microstructure	420 W/cm^2	2.9 MW/m^2 K
Cooke and Kandlikar [2]	Cu	DI water	Microchannel [C_w = 40, 100, 400 μm; f_t = 40, 100, 200 μm; C_h = 192, 208, 273 μm]	DRIE	Microstructure 10×10 mm^2	~1400 kW/m^2	72.3 kW/m^2 K
Cooke and Kandlikar [3]	Cu	DI water	Microchannel [C_w = 197-375-400 μm; C_h = 100-400-445 μm, N = 16, 20, 25]	Machining	Microstructure	250 W/cm^2	270 kW/m^2 K
Ghiu and Joshi [4]	Cu	PF-5060	Microchannel [C_w = 65-105-360 μm, pitch = 0.7 mm, C_h = 0.6 mm]	Automated wafer dicing diamond saw blade	10×10 mm^2	~13 W/cm^2	–
Yu and Lu [5]	Cu	FC-72	Rectangular fin array [S = 0.5, 1, 2 mm; C_h = 0.5, 1, 2, 4 mm]	EDM	10×10 mm^2	980 kW/m^2	~10000 W/m^2 K
Mehta and Kandlikar [6]	Cu alloy 101	Water	Circumferential microchannel [C_h = 0.25–0.3–0.41 mm; C_w = 0.28–0.29–0.40 mm; f_t = 0.21–0.30 mm; pp = 0.5, 0.59, 0.6, 0.7]	CNC	Microstructure	q_{hor} = 1095 kW/m^2 q_{ver} = 1093 kW/m^2	h_{hor} = 129 kW/m^2 K h_{ver} = 109 kW/m^2 K
Mehta and Kandlikar [7]	Cu alloy 101	Water	V-grooves and axial rectangular grooves [C_h = 0.22–0.37–0.51 mm; pitch = 0.39–0.54–0.70 mm; Θ = 45, 60°]	CNC	Microstructure	1070 kW/m^2	h = 96 kW/m^2 K
Patil and Kandlikar [8]	Cu	DI water	Microchannel + microporous coating at fin top [f_w = [a,b]200, 500, 1000 μm; C_w = 300, 400, [a]500, [b]762 μm; C_h = 200, 300, [a,b]400 μm]	Microchannel- CNC, microporous coating- Electrolytic process	Hybrid microstructure [10×10 mm^2]	[a]3250 kW/m^2	[b]995 kW/m^2 K

boiling performance. The dimensions of the channel height, channel base width, channel top width, number of channel and fin tip thickness are tabulated in Table 2. The nomenclature of these microchannels is chosen so as manifest the type and the geometry parameter (β) (e.g. RM-1.0 denotes the Rectangular Microchannel of β = 1). The ratio of channel top width (or channel mouth size) to channel base width (β) for the rectangular microchannel (RM-1.0) is unity whereas parabolic (PM-1.6 and PM-2.0) and stepped microchannels (SM-1.6 and SM-2.0) are tested for β = 1.6 and 2, keeping the channel height constant at 500 μm. Scanning Electron Microscope (SEM) images are shown in Fig. 3 for better understanding of the difference in microchannel profile.

2.3. Experimental procedure

Initially, measured quantity of the distilled water is filled in the boiling vessel. The same quantity of DI water is used in all the experiments. Prior to the test, the DI water is rigorously boiled by the auxiliary heater to remove the dissolved gases. After certain time of degassing, the tests are started by giving incremental heat input to the test surface. The incremental heat input is measured by the wattmeter. After steady state is reached, the saturation temperature and the test surface temperature are recorded and the procedure is repeated for different heat flux values. A closed-loop system of the cooling water pump, pressure transducer and a proportional integral derivative (PID) pressure controller is used to maintain the atmospheric pressure in the chamber. The PID senses the pressure level in the boiling chamber through pressure transducer and compares it with the set value and accordingly it sends the signal to the water pump to supply the cooling water through the condenser coil.

The heater rod and test piece is considered as axisymmetric system. The heat flux from the top surface of the test piece is assumed to be uniform. The heat flux dissipated to the boiling fluid and the surface temperature can be estimated by the three thermocouple readings.

The heat flux from the top test surface is calculated by using Fourier 1-D heat conduction as given in Eq. (1).

$$q'' = -k_{Cu}\frac{dT}{dx} \tag{1}$$

where (dT/dx) is the temperature gradient along the length of the test piece and is calculated by using Taylor's backward series approximation, as in Eq. (2).

$$\frac{dT}{dx} = \frac{3T_1 - 4T_2 + T_3}{2 * \Delta x} \tag{2}$$

where Δ x is the distance between two thermocouples.

The surface temperature of the test piece is calculated by using Eq. (3)

$$T_s = T_1 - q''\left(\frac{x_1}{k_{Cu}}\right) \tag{3}$$

where x_1 is the distance between surface of the test piece and the top thermocouple (T_1) and equal to 2 mm, as shown in Fig. 2.

Heat transfer coefficient (HTC) between the surface and water is estimated by Eq. (4).

$$h = \frac{q''}{(T_s - T_f)} \tag{4}$$

2.4. Visualization of boiling

A high speed camera (AOS Promon 501) at 1000 frames/s with resolution of 320 × 240 pixel is used for visualization of pool boiling. AF NIKKOR 50 mm F/1.4D lens is used. The camera is

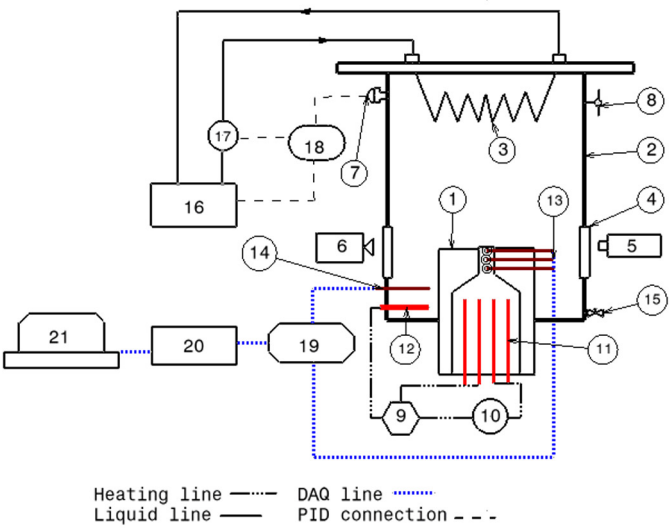

1	Test Section
2	Boiling chamber
3	Condenser coil
4	Sight glass
5	CCD camera
6	Light source
7	Pressure sensor
8	PRV
9	Main Supply
10	Autotransformer
11	Main cartridge heaters
12	Auxiliary heater
13	Test section thermocouples
14	Bulk Fluid thermocouple
15	Drain
16	Water tank
17	Pump
18	PID
19	Signal conditioner
20	DAQ
21	Workstation

Fig. 1. Schematic diagram of experimental setup.

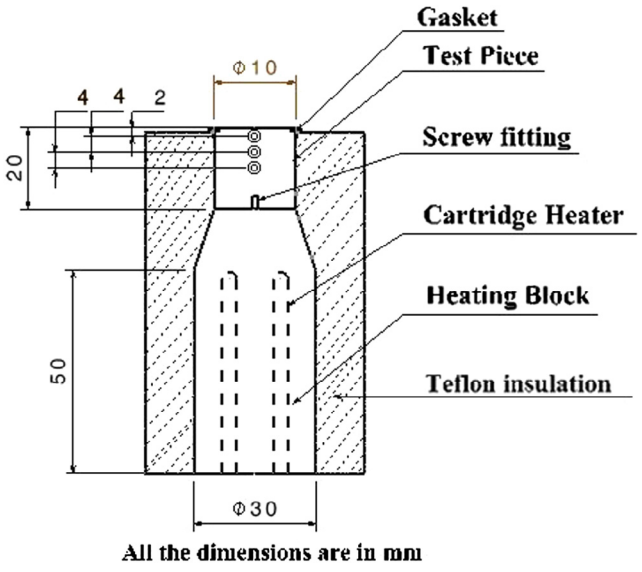

Fig. 2. Test section.

positioned in front of the sight glass. A diffused light source is placed opposite to the camera to provide uniform illumination on the test surface. Promon studio viewer software interfaces the camera with PC. This software is used to control triggering and recording the videos and it is also used to set the shutter speed, pixel size, and frame rate of the videos to be captured. These recorded sequences are marked as per the requirement and converted into images. These images are processed in MATLAB image processing tool to measure the horizontal (a) and vertical dimension (b) of the bubble meniscus in terms of pixels. The actual value of a and b is obtained, as given in Eq. (5-a), by the knowledge known size of object and its corresponding pixels. The spherical shape of the bubble slightly turns to elliptical profile at its bottom, as shown in Fig. 4 and thus measurement of the bubble departure diameter requires certain assumption to obtain the equivalent bubble diameter. As suggested by Siegel and Keshock [9], the bubble departure diameter (D_b) is estimated as the arithmetic mean of a and b, as given in Eq. (5-b).

$$\text{a or b} = \frac{\text{No. of pixels of captured image} \times \text{Actual size of reference object}}{\text{No. of pixels of reference object}} \tag{5-a}$$

$$D_b = \frac{a+b}{2} \tag{5-b}$$

The number of bubbles generated and departed from the same nucleation site per second is called as bubble frequency. Bubble frequency (f), as given in Eq. (6), is the reciprocal of sum of waiting period and growth period of the bubble. The representative value of bubble departure diameter and bubble frequency is taken from the average measurement of the 30 consecutive bubbles.

$$f = \frac{1}{(t_w + t_g)} \tag{6}$$

Table 2
Dimensions of microchannel geometries.

Test surface	Type	Channel base width, Wb (μm)	Channel top width, Wt (μm)	Channel height, Ch (μm)	Fin tip thickness, ft (μm)	No of channel	Ratio channel top to base width (β)
Plain-0	Plain	–	–	–	–	0	0
RM-1.0	Rectangular	500	500	500	500	9	1
PM-1.6	Parabolic	500	800	500	200	9	1.6
PM-2.0	Parabolic	250	500	500	250	13	2
SM-1.6	Stepped	500	800	500	200	9	1.6
SM-2.0	Stepped	250	500	500	250	13	2

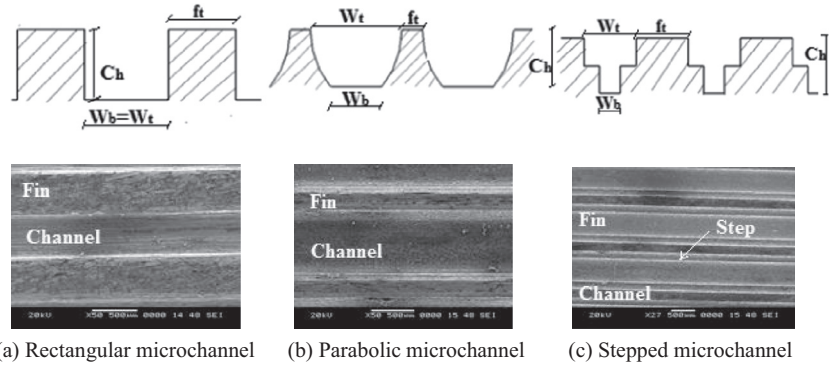

(a) Rectangular microchannel (b) Parabolic microchannel (c) Stepped microchannel

Fig. 3. Microchannel geometries.

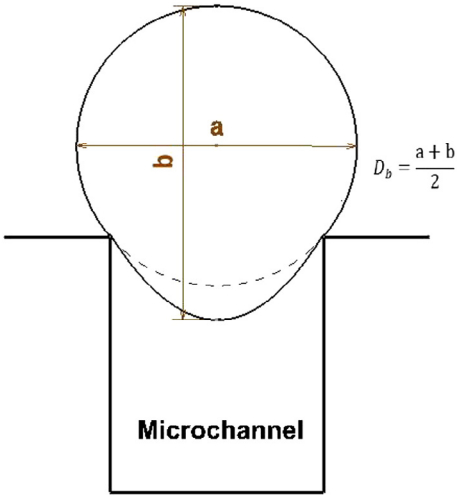

Fig. 4. Measurement of equivalent bubble departure diameter.

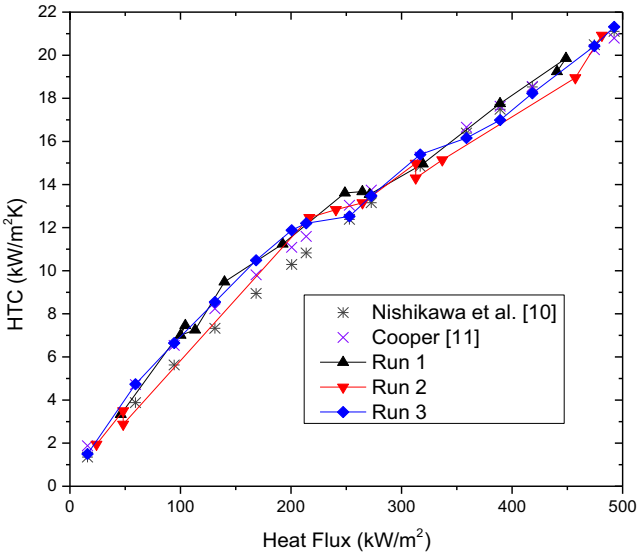

Fig. 5. Repeatability and validation of the experimental setup.

Time taken by the bubble to grow from its nucleation to the departure is called growth period (t_g) and time taken for nucleation of the next bubble after the departure of preceding bubble from the same site is called waiting period (t_w).

2.5. Experimental uncertainty

Thermal conductivity of copper, thermocouple calibration and thermocouple location measurement are considered in the uncertainty calculations of the heat flux and surface temperature by propagation of error method. The uncertainty of the thermal conductivity of copper is 2.33% throughout the operating temperature. The uncertainty in temperature measurement is ±0.1 °C. Uncertainty in distance measurement is ±0.0001 m. The uncertainty in the heat flux is calculated by using Eq. (7). Dividing these calculated values by the heat flux values yields the percentage uncertainty and it is found to be 8.07% at higher operating temperature.

$$U_{q''} = \left[\left(\frac{q''}{k_{Cu}}U_{k_{Cu}}\right)^2 + \left(\frac{3k_{Cu}}{2\Delta x}U_{T_1}\right)^2 + \left(\frac{4k_{Cu}}{2\Delta x}U_{T_2}\right)^2 + \left(\frac{k_{Cu}}{2\Delta x}U_{T_3}\right)^2 + \left(\frac{q''}{\Delta x}U_{\Delta x}\right)^2\right]^{1/2} \quad (7)$$

The uncertainty in the surface temperature, obtained by Eq. (8), lies between 0.14 °C and 0.17 °C throughout the experiments.

$$U_{T_s} = \left[(U_{T_1})^2 + \left(\frac{x_1}{k_{Cu}}U_{q''}\right)^2 + \left(\frac{q''}{k_{Cu}}U_{\Delta x}\right)^2 + \left(\frac{q''x}{k_{Cu}^2}U_{k_{Cu}}\right)^2\right]^{1/2} \quad (8)$$

The uncertainty in the HTC is calculated by using Eq. (9) and it is found to be 8.19% at higher operating temperature.

$$U_h = \left[\left(\frac{U_{q''}}{T_s - T_f}\right)^2 + \left(\frac{q''}{(T_s - T_f)^2}U_{T_s}\right)^2 + \left(\frac{q''}{(T_s - T_f)^2}U_{T_f}\right)^2\right]^{1/2} \quad (9)$$

The uncertainty in the measurement of bubble departure diameter (U_{D_b}) is 0.05 mm. The maximum uncertainty in the bubble frequency (U_f) is estimated to be 10.45%.

3. Experimental results

3.1. Repeatability and validation

In order to examine the reproducibility and repeatability of the experimental data, three pre-experimental runs are taken with distilled water at atmospheric pressure for plain surface (Plain-0). HTC versus heat flux for these runs are plotted as shown in Fig. 5 which confirm the repeatability of the experimental data. To validate the experimental results, HTC values obtained during run-3 on the plain surface are compared with the predicted values obtained from the correlation of Nishikawa et al. [10] and Cooper [11]. The average deviation between measured and predicted

HTC values obtained by the correlation of Nishikawa et al. and Cooper is found to be 15.22% and 5%, respectively.

3.2. Effect of microchannel geometries on boiling heat transfer

Fig. 6 shows the comparison of boiling curves for plain surface and different microchannel geometries. All the tested microchannel geometries have augmented the heat transfer. It is observed that modification in the rectangular channel (RM-1.0) into the parabolic (PM-1.6 & Para-2.0) and stepped channel (SM-1.6 & 2.0) has remarkably increased the heat transfer. Heat transfer from PM-1.6, PM-2.0, SM-1.6, and SM-2.0 is 38.6%, 88%, 169%, and 59.15%, higher than that of the RM-1.0 at 11.7 °C wall superheat, respectively. The augmentation in the heat transfer may be the consequence of enhanced microlayer evaporation, increased bubble diameter and improved bubble frequency. SM-1.6, a stepped microchannel, has the best heat transfer performance among the tested microchannel geometries. The stepped channel profile has higher heat transfer rate for β = 1.6 compared to that of β = 2.0 whereas parabolic channel profile has higher heat transfer for β = 2.0 compared to that of β = 1.6. Compound study of bubble departure diameter and bubble frequency can justify this contradiction. The channel profile has an influence on heat transfer rate as the heat transfer rate from SM-1.6 is higher than PM-1.6. The heat transfer from PM-2.0 is slightly higher than the SM-2.0. These facts are explained in detail in Section 4. The incipient temperature values are given in Table 3. Compared to Plain-0, 23.18% reduction in the incipient temperature is noticed for SM-1.6. The HTC at different heat flux values are plotted in Fig. 7. Higher HTC is observed for SM-1.6 which indicates the better performance of SM-1.6 amongst all the tested surfaces. At heat flux of 100 kW/m^2, the HTC of RM-1.0, PM-1.6, PM-2.0, SM-1.6 and SM-2.0 is found to be 25.9%, 21.49%, 24.62%, 35.37%, and 23.88% higher than that of the Plain-0, respectively. The difference between HTC of the stepped microchannel and rectangular microchannel increases with increase in the heat flux. Non-linear relationship between HTC and heat flux is observed for all microchannel geometries and it is expressed as- $h = 0.23 \times q^{0.8}$ for SM-1.6.

The variation in the Jakob number at different heat fluxes for all the test surfaces is shown in Fig. 8. An empirical relation between Jakob number (Ja), $\rho_l C_{pl} \Delta T / \rho_v h_{fg}$, and heat flux is given by McHale and Garimella [12] for smooth surface, as in Eq. (10-a). The present experimental values of Plain-0 are in good agreement with this relation. The empirical relation obtained for SM-1.6 from the present work is given in Eq. (10-b). Since such relationship is not present in the literature for microchannel geometries, this may be of use to predict Ja at known heat fluxes. At low heat flux, it is found that Jakob number changes rapidly with small change in the heat

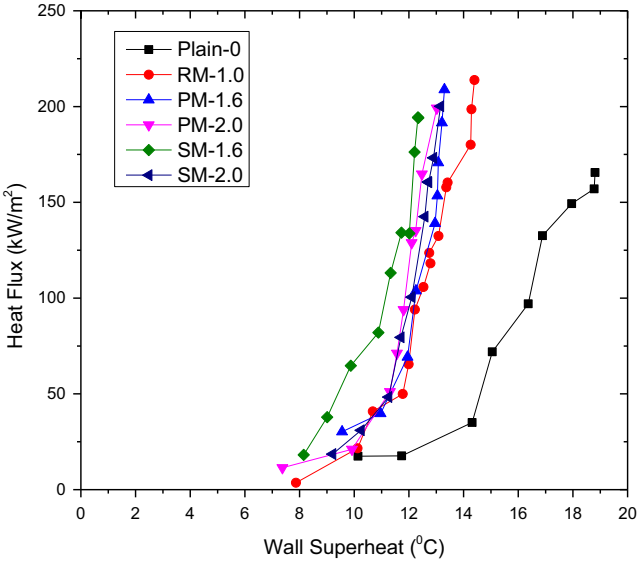

Fig. 6. Boiling curves of plain and different microchannel geometries.

Table 3
Incipient temperature.

Test surface	Incipient temperature, °C
Plain-0	11.73
RM-1.0	10.12
PM-1.6	9.55
PM-2.0	9.91
SM-1.6	9.01
SM-2.0	9.21

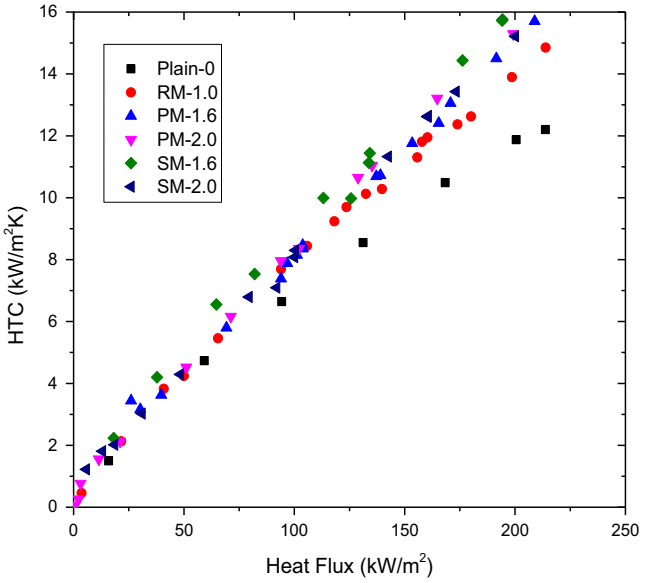

Fig. 7. HTC of tested geometries at different heat flux values.

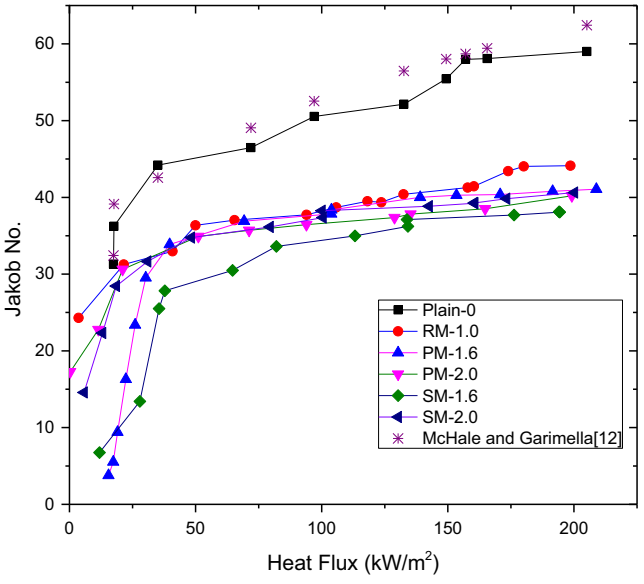

Fig. 8. Variation of Jakob No. with Heat flux for all test surfaces.

flux. Jakob number remains almost constant for all the microchannel geometries at high heat flux range which indicates the dominance of latent heat transfer from the microchannel geometries.

For Plain surface [12] : $Ja = 19.35 \times q^{0.23}$ (10-a)

For SM-1.6[Present work] : $Ja = 8.0 \times q^{0.3}$ (10-b)

4. Bubble dynamics

4.1. Mechanism of bubble growth

The bubble growth study for all the test surfaces is done by the visualization of bubble nucleation, intermediate bubble growth and bubble departure at different heat fluxes. The time trace of the bubble diameter is presented in Table. 4 at q = 160–175 kW/m^2. It is found that for all the microchannel geometries bubble generates at the corner of the channel, enlarges in the channel space and finally grows vertically. It is also noticed that bubble generates at the top of the fin and departs independently at low heat flux. At high heat flux, horizontal coalescence is observed between the bubbles generated from the adjacent channel as it grows beyond the channel height. A vertical coalescence rarely occurs between the bubble generated at the channel base and top of the fin.

As shown in Fig. 9, the parabolic and stepped microchannel can have larger channel top width than rectangular one by keeping the same channel base width and channel height. Thus, the effect of channel top width on the bubble growth and departure diameter is discussed further. Larger channel mouth assist the growth of the bubble which has been generated from the small cavities present at the channel base. In case of rectangular microchannel (β = 1), bubble is confined between the two walls and cannot grow beyond the channel width. During this phase, bubble may grow laterally along the length of channel and turns into elliptical shape. Finally, making a finite angle with top of the fin, bubble takes mushroom shape as it grows beyond the channel height and departs spherically, as shown in Fig. 10(a). The liquid supply to the nucleation site for different channel profiles is schematically shown in Fig. 10(b).

Table 4
Bubble growth report at q = 160–175 kW/m^2.

Test surface	Bubble ebullition	Intermediate bubble growth		Bubble departure
Plain-0	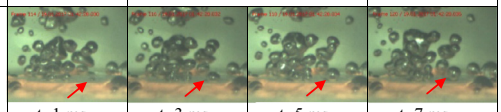 t=1 ms d=0.2 mm	t=3 ms d=0.39 mm	t=5 ms d=0.82 mm	t=7 ms D_b=1.5 mm
RM-1.0	 t=1 ms d=0.42 mm	t=2 ms d=1.03 mm	t=4 ms d=1.80 mm	t=6 ms D_b=1.85 mm
PM-1.6	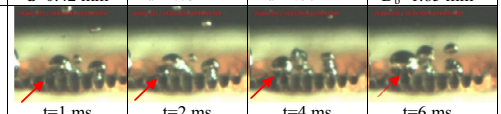 t=1 ms d=0.74 mm	t=2 ms d=1.32 mm	t=4 ms d=1.75 mm	t=6 ms D_b=1.97 mm
PM-2.0	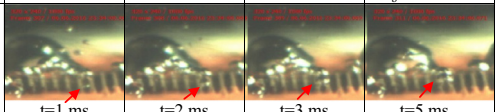 t=1 ms d=0.35 mm	t=2 ms d=1.34 mm	t=3 ms d=1.58 mm	t=5 ms D_b =1.63 mm
SM-1.6	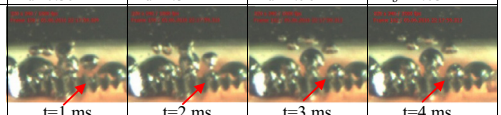 t=1 ms d=0.57 mm	t=2 ms d=0.98 mm	t=3 ms d=2.1 mm	t=4 ms D_b=2.01 mm
SM-2.0	 t=1 ms d=0.35 mm	t=2 ms d=0.85 mm	t=4 ms d=1.6 mm	t=5 ms D_b=1.70 mm

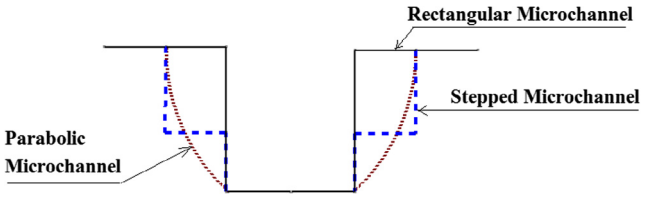

Fig. 9. Schematic diagram of different channel profile.

Since, parabolic and stepped microchannel have higher channel top width, trend of the bubble growth is found to be different. In both cases, bubble grows spherically in the channel zone before departure. However, bubble turns to mushroom shape as parabolic wall profile offers the restriction to the vertical bubble growth. This indicates the existence of cohesive role of the channel profile and channel top width of the geometry for the enhancement in departure diameter and bubble frequency.

4.2. Bubble departure diameter

The accuracy of the bubble departure diameter of plain surface is examined by comparing experimental values with that of the correlation of Cole [13], as shown in Fig. 11. The mean absolute error (MAE), obtained by Eq. (11), between experimental and predicted values is found to be 16.53%. Cole [13] have studied the bubble dynamics on the polished zirconium ribbon using n—pentane and water at atmospheric and sub-atmospheric pressure, respectively. The variation in the experimental and predicted values of the bubble departure diameter is the consequence of difference in experimental conditions and surface topography of the test piece used in the present study and that of Cole [13].

$$MAE = \frac{1}{n}\sum \frac{|D_{b_{pred}} - D_{b_{exp}}|}{D_{b_{exp}}} \times 100 \quad (11)$$

The experimental and predicted values of bubble departure diameter from the correlation of Jensen and Memmel [14], Ruckenstein [15] and Hatton and Hall [16] are presented at different Jakob numbers in Fig. 12. The predicted values from these correlations have a linear relationship between bubble departure diameter and Jakob number with different slope. It is noticed that bubble departure diameter of all the tested microchannels is a function of Jakob number.

The bubble diameter of stepped microchannel SM-1.6 and SM-2.0 are found to be closer with the predicted values of Hatton and Hall [16] correlation. They have considered the influence of surface conditions on bubble diameter but unlike to their study, the role of surface tension force and bubble inertia force during unsteady bubble growth seems to be important in case of microchannel surfaces. This may be a reason for the variation in the experimental and predicted bubble departure diameter values. The bubble departure diameter is found to be 1.7 ± 0.3 mm for all the microchannel geometries. At high heat flux range, the bubble departure diameter of SM-1.6 is 30.96% larger than that of Plain-0.

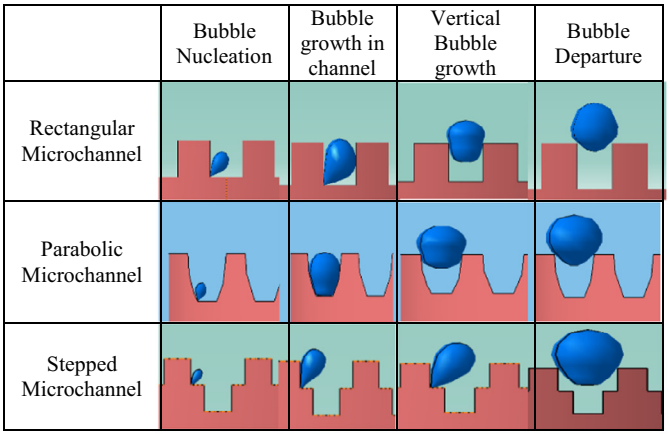

Fig. 10. Proposed mechanism of (a) bubble growth and (b) liquid supply in the microchannel.

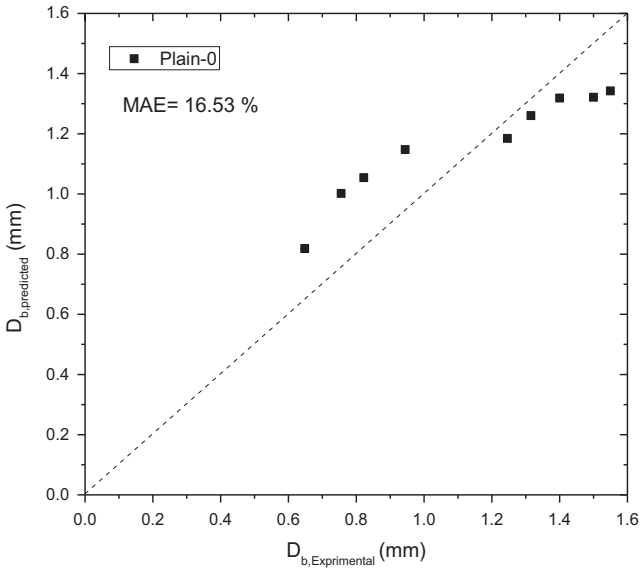

Fig. 11. Comparison of bubble departure diameter of Plain-0 with the correlation of Cole [12].

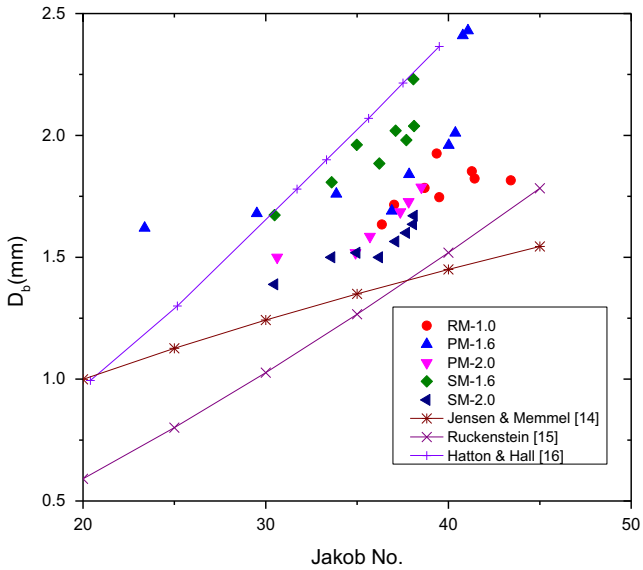

Fig. 12. Variation of bubble departure diameter with Jakob No.

4.3. Bubble frequency

The experimental values of bubble frequency for all the geometries at different Jakob number is plotted in Fig. 13. It is observed that the bubble frequency increases rapidly with increase in the Jakob number for all the microchannel geometries. The identical trend of the bubble frequency is reported by McHale and Garimella [12]. Bubble frequency is reciprocal of the sum of growth period and waiting time of the bubble. The increase in the wall superheat triggers the nucleation of the bubble from the activated site which leads to drastic reduction in the waiting time. The surface tension decreases linearly with increase in the temperature which results in the reduction of bubble growth period. Thus increase in bubble frequency with increase in Jakob number is the consequence of decrease in growth period and waiting time. The frequency of the bubble formation on PM-2.0 and SM-2.0 is found to be similar at different Jakob numbers. At 130 kW/m^2, the bubble frequency for SM-1.6 is increased by 104% compared to that of Plain-0.

4.4. Effect of microchannel profile on bubble departure diameter

A pioneering study is done by the authors to examine the role of channel profile on bubble diameter, frequency and growth rate. The bubble departure diameter of the microchannel at different heat flux is plotted in Fig. 14 for $\beta = 1.0$, $\beta = 1.6$ and $\beta = 2.0$. The

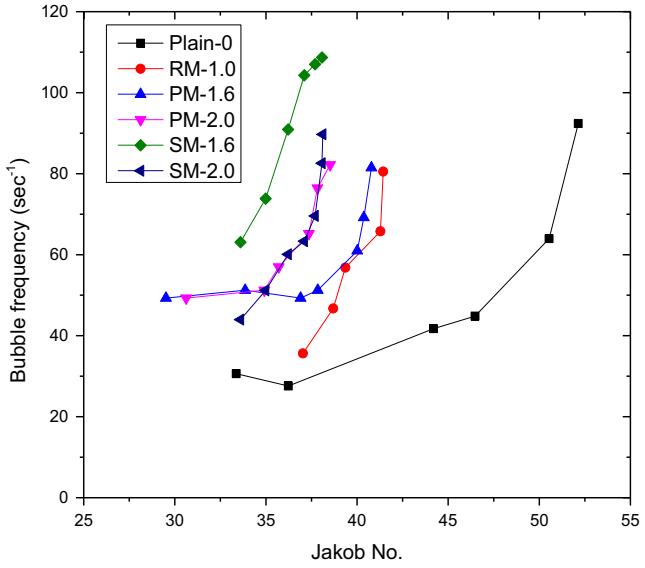

Fig. 13. Variation of bubble frequency with Jakob No.

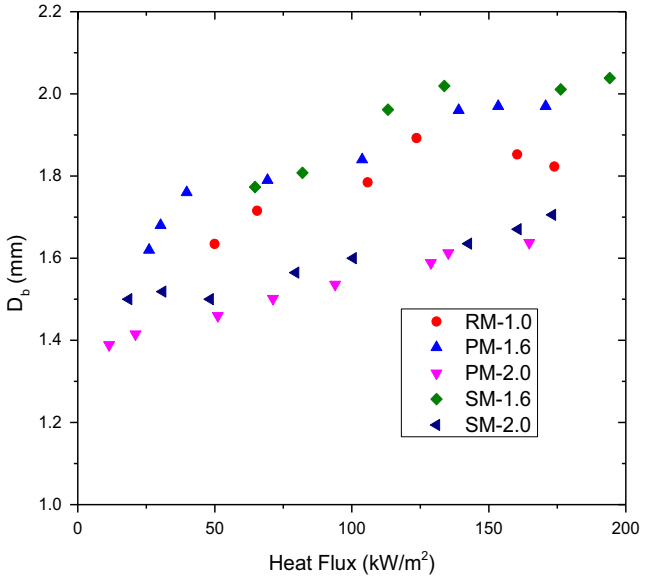

Fig. 14. Variation of the bubble departure diameter of the microchannel with the heat flux.

bubble departure diameter is found to be strong function of heat flux as well as channel profile. It is observed that stepped microchannel for both the cases (β = 1.6 and 2.0) has higher bubble departure diameter than the parabolic channel profile. The potential of microlayer evaporation is considered to study the influence of channel profile. The wetted surface area of the stepped profile is higher than the parabolic profile which ensures the higher potential of microlayer evaporation. The superheated liquid supply to the nucleation site at the step of the channel is possible from the either side of the channel wall, as shown in Fig. 10(b). This increases the quantity of the liquid evaporation and thus bubble departed from the stepped microchannel is largest amongst all tested geometries.

4.5. Effect of microchannel profile on bubble frequency

The bubble growth study including the forces acting on the bubble are considered to analyze the effect of channel profile on

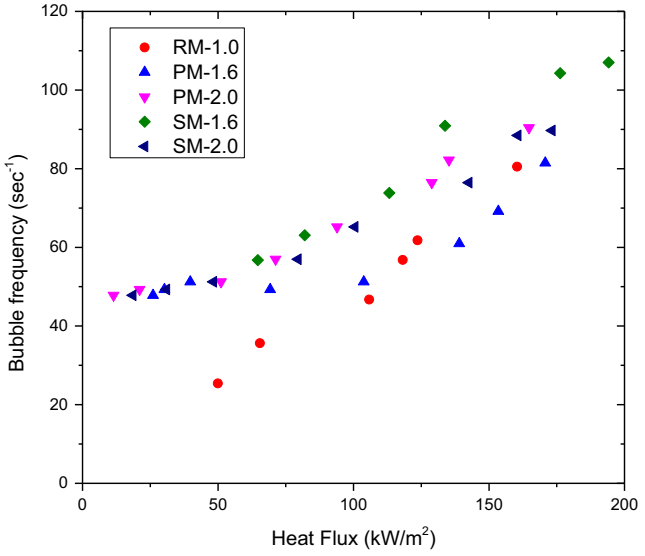

Fig. 15. Variation in the bubble frequency of the microchannel with the heat flux.

the bubble frequency. The bubble frequency of the microchannel geometries at different heat flux is shown in Fig. 15 for β = 1.0, β = 1.6 and β = 2.0. Bubble frequency of RM-1.0 is found to be lowest at low heat flux value as the bubble growth period is much higher than other microchannel geometries. Bubble frequency of RM-1.0 increases rapidly with increase in the heat flux. For β = 1.6, bubble frequency of the stepped microchannel (SM-1.6) is higher than the parabolic microchannel (PM-1.6). For wider parabolic microchannel, it is observed that bubble acquires the exact shape of the wall profile and adheres to the solid wall. The surface tension force seems to be higher in this case. Thus, it reduces the bubble growth rate and frequency of the bubble formation. The bubble morphology of the stepped microchannel (SM-1.6) is different than parabolic (PM-1.6). Bubble generated at the step of the channel can grow without much influence of the channel wall. Bubble nucleated at the base of the channel exerts a push force to the growing bubble at the next step of the same channel which results in higher bubble frequency. It is found that bubble frequency PM-2.0 is higher than that of PM-1.6, as shown in Fig. 15. It seems that the time taken by the bubble to grow in the parabolic channel space is a key parameter which affects the bubble frequency. PM-2.0 has narrow channel width and hence bubble can quickly grows in its channel space followed by the vertical growth above the channel height. This rapid bubble growth leads to formation of bubble neck and thus bubble departs relatively smaller in size. Since the bubble frequency has remarkable role in heat transfer mechanism, heat transfer from SM-1.6 and PM-2.0 is higher than that of the SM-2.0 and PM-1.6, respectively. The marginal difference in the bubble frequencies of PM-2.0 and SM-2.0 is observed which may have resulted in the slightly higher heat transfer from the PM-2.0 than that of the SM-2.0. At 130 kW/m^2, the bubble frequency of SM-1.6 increased by 104% compared to Plain-0.

5. Modeling of bubble departure diameter

5.1. Force balance

In the microchannel geometries, the bubble nucleates and grows because of the evaporation of liquid microlayer present on the channel surface and this growth must be driven by inertia, as discussed by Ramaswamy et al. [17]. As mentioned earlier, the bubble departing from the channel wall is considered to be

spherical and it makes a finite contact angle with the top surface of the channel wall. Hence, surface tension force should be considered to estimate the bubble diameter. The model developed in the present work for prediction of bubble departure diameter from the microchannel geometries considers the unsteady growth force, buoyancy force, surface tension, lift force and bubble inertia. The expression for the different forces are given below

(i) Unsteady growth force (F_{duy}): The bubble growth is a dynamic process for which momentum transfer between the growing bubble and surrounding stagnant liquid should be considered. The unsteady growth force acting on the growing bubble can be solved by estimating the pressure distribution along the liquid–vapor interface. The expression of growth force, given in Eq. (12), considering transient bubble growth was developed by Zeng et al. [18].

$$F_{duy} = \pi\rho_l r^2\left(\frac{3}{2}C_s\dot{r}^2 + r\ddot{r}\right) \tag{12}$$

where C_s is an empirical constant and is equal to 20/3 as suggested by Klausner et al. [19] and r is an instantaneous radius of the bubble.
For inertia driven mechanism, bubble growth rate follows Eq. (13).

$$r(t) = at \tag{13}$$

where a is a function of wall temperature and fluid property. Thus, expression for unsteady growth force is formulated as Eq. (14).

$$F_{duy} = \frac{3}{2}\rho_l\pi a^2 C_s r^2 \tag{14}$$

(ii) Buoyancy force (F_{buy}): The upward force experienced by the growing bubble due to density variation between liquid and vapor is defined as buoyancy force and is obtained by Eq. (15).

$$F_{buy} = (\rho_l - \rho_v)gV_b \tag{15}$$

where V_b is the volume of spherical bubble and is obtained by Eq. (16).

$$V_b = \frac{\pi}{6}D_b^3 \tag{16}$$

(iii) Surface tension force (F_{st}): Surface tension force acting on the bubble is formulated by considering the trend of the bubble growth. During phase-I growth, as shown in Fig. 16, bubble grows on the base of channel where it expands vertically upward. After certain time, bubble grows against the confined channel wall. During Phase-II bubble growth, bubble turns into spherical shape where bubble meniscus makes a contact with the channel top. Surface tension forces involved in Phase-I $(F_{st})_I$ and Phase-II growth $(F_{st})_{II}$ period are considered as a function of channel parameter, surface tension, contact angle and bubble departure diameter and is formulated as given in Eq. (17).

$$F_{st} = (F_{st,y})_I + (F_{st,y})_{II} = \frac{\pi}{3}\sigma\left[\frac{2W_b^2}{9C_h} + \frac{W_t^2}{D_b}\right] \tag{17}$$

where $(F_{st,y})_I$ and $(F_{st,y})_{II}$ are the y-component of the surface tension forces acting during the Phase-I and Phase-II growth, respectively.

(iv) Lift force (F_L): The non-uniform velocity field is present across the bubble due to channel confinement, the liquid supply through channel and wake of the departing bubble. Hence, bubble experiences the upward lift force which is estimated by Eq. (18) as given in Ramaswamy et al. [17].

$$F_L = 2\pi\rho_l C_l(aD_b)^2 \tag{18}$$

where $C_l = 1.2$.

(v) Bubble inertia force (F_{bi}): The bubble inertia force resist the dynamic bubble growth which is obtained by Eq. (19), as suggested by Sharma [20].

$$F_{bi} = d(m_b v_b) = m_b\frac{dv_b}{dt} + v_b\frac{dm}{dr}\frac{dr}{dt} \tag{19}$$

where $v_b = \frac{dr}{dt} = a$, $\frac{dv_b}{dt} = \frac{d\dot{r}}{dt} = 0$, $\frac{dm}{dr} = \frac{\pi}{3}\rho_b D_b^2$.
Combining above terms, the expression of the resultant bubble inertia force is given in Eq. (20).

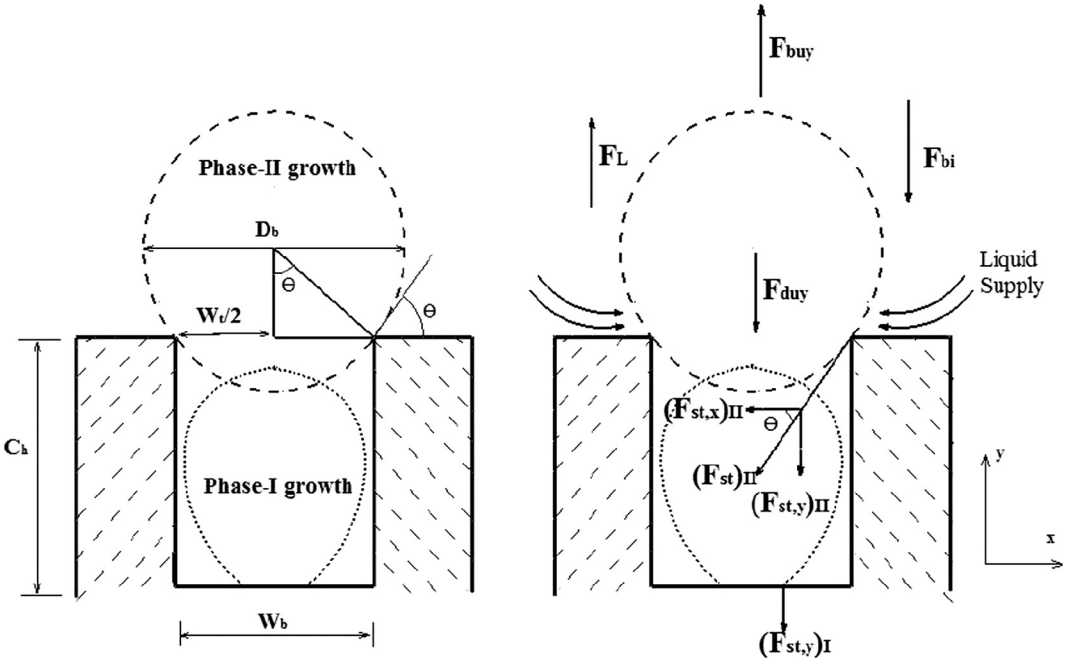

Fig. 16. Bubble growth in Rectangular Microchannel.

$$F_{bi} = a^2 \frac{\pi}{3} \rho_b D_b^2 \quad (20)$$

As suggested by Ramaswamy et al. [17], the liquid inertia force is considered as zero as velocity of bubble is constant.
The force balance equation can be written as Eq. (21).

$$F_{duy} + F_{st} + F_{bi} = F_{buy} + F_L \quad (21)$$

The schematic description of the forces acting on the growing bubble is shown in the Fig. 16. It is observed that surface tension force is dominant during the initial growth of the bubble whereas it is found to be negligible during the Phase-II growth because of gradual reduction in the line of contact between the bubble and channel wall. As bubble grows in the channel space, considerable velocity and pressure variation exists across the bubble meniscus. During the Phase-II growth, buoyancy force become dominant as bubble diameter increases. The spherical bubble departs from the channel as upward forces (buoyancy and lift force) dominate the downward acting forces (growth force, surface tension and inertia force).

5.2. Verification of the model

Cooke and Kandlikar [3] carried out pool boiling experiments on rectangular microchannel at atmospheric condition of DI water. Bubble departure diameter for Chip-2 ($W_b = W_t = 197$ μm and $C_h = 335$ μm) and Chip-9 ($W_b = W_t = 375$ μm and $C_h = 400$ μm) was found to be 0.82 mm and 1.55 mm, respectively. However, the corresponding wall superheat or heat flux is not available in the literature. Hence, bubble departure diameter is considered to be constant throughout their experiments. The bubble departure diameter of Chip-2 and Chip-9 is predicted by present model and results are presented in Fig. 17. It is found that the predicted bubble departure diameter is in good agreement with the experimental results of Cooke and Kandlikar [3] with MAE of 3.33% and 38.21% for Chip-9 and Chip-2, respectively. The deviation between predicted and experimental bubble departure diameter of Chip-2 is in the range of 0.27–0.30 mm. The bubble growth along the channel length may be much higher in the narrow channel of Chip-2 ($W_b = 197$ μm). The surface tension forces during lateral elongation of the meniscus is not considered in the present model. This may be the reason for the over prediction of the bubble diameter in case of Chip-2.

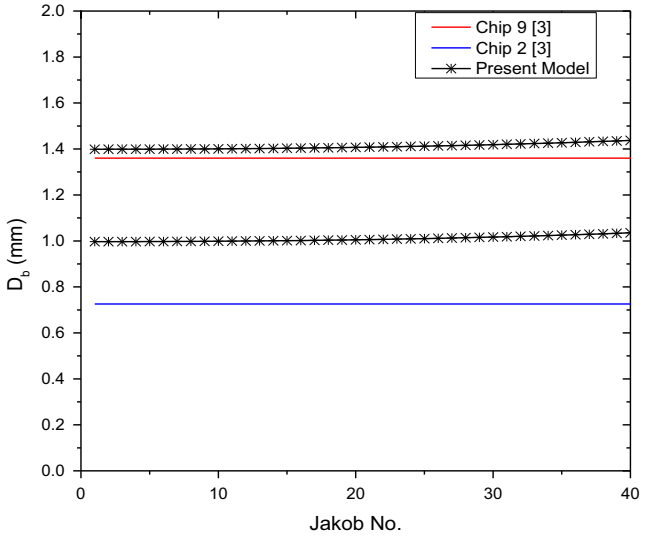

Fig. 17. Comparison of bubble departure diameter of Chip 2 and 9 [3] with the present model.

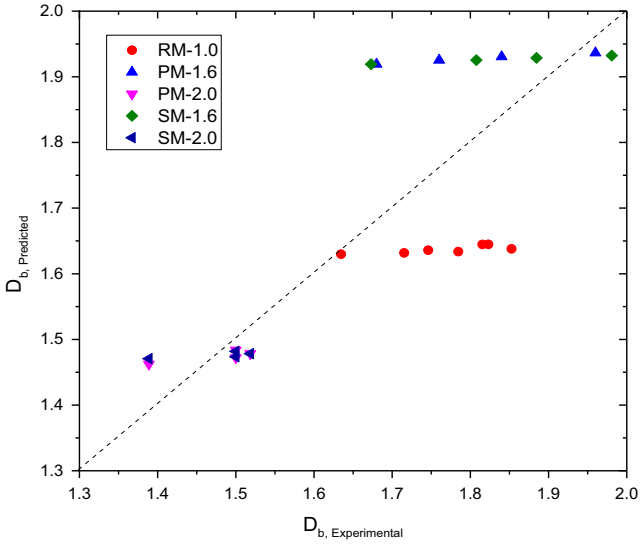

Fig. 18. Comparison of predicted and experimental bubble departure diameter of microchannel geometries.

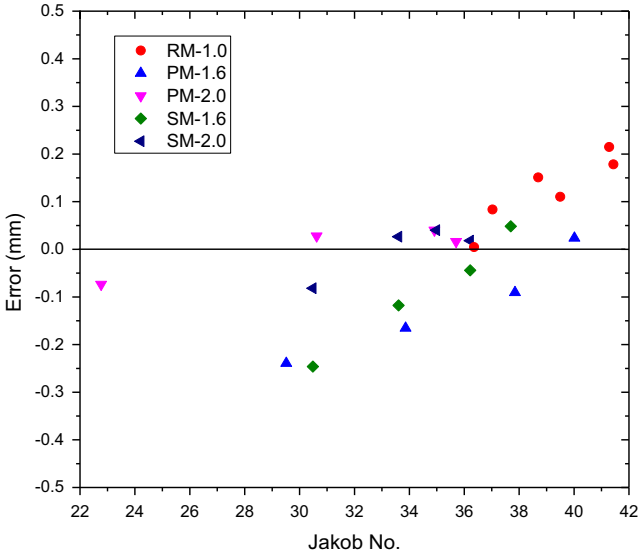

Fig. 19. Error between experimental and predicted bubble departure diameter of microchannel geometries.

The bubble departure diameter predicted by the present model and measured during experimentation is compared and plotted in Fig. 18 for all the microchannel geometries. MAE between predicted and experimental bubble departure diameter values for all the microchannel geometries is found to be 5.58%. The error in the predicted bubble departure diameter for tested microchannel geometries is shown in Fig. 19. The error between experimental and predicted bubble departure diameter is found to be ±0.25 mm.

6. Conclusion

The potential of rectangular, parabolic and stepped microchannel as a heat dissipating device was experimentally examined for low heat flux applications at saturated condition of distilled water. The effect of channel profile and geometrical parameter on bubble departure diameter and bubble frequency was studied by high speed visualization technique. The wall force acting on the growing

bubble was found to be influenced by the channel profile and channel top width. The improved liquid supply in the stepped microchannel having wider channel top width has resulted in the enhanced microlayer evaporation and weaker wall force. Thus higher heat transfer from SM-1.6 was noticed compared to all the tested microchannels. Following conclusions are drawn from this study.

i. Heat transfer from the RM-1.0 was 182.8% higher than that of the Plain-0 at 11.7 °C wall superheat.
ii. Compared with the rectangular microchannel, 38.6% and 169% heat transfer enhancement was estimated at 11.7 °C wall superheat from PM-1.6 and SM-1.6, respectively.
iii. The bubble departure diameter was found to be 1.7 ± 0.3 mm for all the microchannel geometries which is approximately 21.42% higher than that of Plain-0.
iv. The force balance approach was used to estimate the bubble departure diameter for the microchannel geometries and it was found to be in good agreement with the measured bubble diameter values with MAE of 5.58%.

Acknowledgement

Authors would like to acknowledge the financial support extended by the Council of Scientific and Industrial Research (CSIR), India, (sanction order 22/661/14/EMR-II) to carry out this research work. Authors would also like to acknowledge Centre for System Design (CSD): A Centre of Excellence at NITK, Surathkal for the provision of DAQ facility. The technical support received from members of SOLVE: The Virtual Lab @ NITK Surathkal (csd.nitk.ac.in) is deeply appreciated.

References

[1] Arvind Jaikumar, S. Kandlikar, Ultra-high pool boiling performance and effect of channel width with selectively coated open microchannel, Int. J. Heat Mass Transf. 95 (2016) 795–805.
[2] Dwight Cooke, Satish G. Kandlikar, Pool boiling heat transfer and bubble dynamics over plain and enhanced microchannel, J. Heat Transf. 133 (5) (2011) 1–9.
[3] Dwight Cooke, Satish G. Kandlikar, Effect of open microchannel geometry on pool boiling enhancement, Int. J. Heat Mass Transf. 55 (2012) 1004–1013.
[4] Camil-Daniel Ghiu, Yogendra K. Joshi, Visualization study of pool boiling from thin confined enhanced structures, Int. J. Heat Mass Transf. 48 (2005) 4287–4299.
[5] Chih Kuang Yu, Ding Chong Lu, Pool boiling heat transfer on horizontal rectangular fin array in saturated FC-72, Int. J. Heat Mass Transf. 50 (2007) 3624–3637.
[6] Jeet S. Mehta, Satish G. Kandlikar, Pool boiling heat transfer enhancement over cylindrical tubes with water at atmospheric pressure, Part I: experimental results for circumferential rectangular open microchannel, Int. J. Heat Mass Transf. 64 (2013) 1205–1215.
[7] Jeet S. Mehta, Satish G. Kandlikar, Pool boiling heat transfer enhancement over cylindrical tubes with water at atmospheric pressure, Part II: experimental results and bubble dynamics for circumferential V-groove and axial rectangular, Int. J. Heat Mass Transf. 64 (2013) 1216–1225.
[8] Chinmay M. Patil, Satish G. Kandlikar, Pool boiling enhancement through microporous coatings selectively electrodeposited on fin tops of open microchannel, Int. J. Heat Mass Transf. 79 (2014) 816–828.
[9] R. Siegel, E.G. Keshock, Effects of reduced gravity on nucleate boiling bubble dynamics in saturated water, AIChE J. 10 (4) (1964) 509–517.
[10] K. Nishikawa, Y. Fujita, H. Ohta, S. Hidaka, Effect of the surface roughness on the nucleate boiling heat transfer over the wide range of pressure, Proceedings of the 7th International Heat Transfer Conference, Munich, Germany, vol. 4, 1982, pp. 61–66.
[11] M.G. Cooper, Saturation nucleate pool boiling-a simple correlation, in: National Conference on Heat Transfer, Permagon Press, Elmsford, NY, 1984, pp. 785–793.
[12] John P. McHale, Suresh V. Garimella, Bubble nucleation characteristics in pool boiling of a wetting liquid on smooth and rough surfaces, Int. J. Multiph. Flow 36 (2010) 249–260.
[13] R. Cole, Frequency and departure diameter at sub-atmospheric pressures, Am. Inst. Chem. Eng. J. 13 (1967) 779–783.
[14] M.K. Jensen, G.J. Memmel, Evaluation of bubble departure diameter correlations, Proceedings of the Eighth International Heat Transfer Conference, vol. 4, 1986, pp. 1907–1912.
[15] E. Ruckenstein, A physical model for nucleate boiling heat transfer from a horizontal surface, Buletinul Inst. Polit. Bucuresti (Romania) 23 (1961) 79–88.
[16] A. Hatton, I. Hall, Photographic study of boiling on prepared surfaces, in: S. Siva (Ed.), Proceedings of 3rd International Heat Transfer Conference, vol. 4, 1966, pp. 24–37.
[17] C. Ramaswamy, Y. Joshi, W. Nakayama, W.B. Johnson, Semi-analytical model for boiling from enhanced structures, Int. J. Heat Mass Transf. 46 (2003) 4257–4269.
[18] L.Z. Zeng, J.F. Klausner, R. Mei, A unified model for the prediction of bubble detachment diameters in boiling systems-I pool boiling, Int. J. Heat Mass Transf. 36 (9) (1993) 2261–2270.
[19] J.F. Klausner, R. Mei, D.M. Bernhard, L.Z. Zeng, Vapor bubble departure in forced convection boiling, Int. J. Heat Mass Transf. 36 (3) (1993) 651–662.
[20] P.R. Sharma, Determination of heat transfer rates in nucleate pool boiling of pure liquids for a wide range of pressure and heat flux, Proceedings of the 11th International Heat Transfer Conference, Kyongju, South Korea, vol. 2, 1998, pp. 467–472.